Science Advances
AAAS

advances.sciencemag.org/cgi/content/full/6/29/eabb2307/DC1

Supplementary Materials for

Compact nanoscale textures reduce contact time of bouncing droplets

Lin Wang, Ruoxi Wang, Jing Wang, Tak-Sing Wong*

*Corresponding author. Email: tswong@psu.edu

Published 17 July 2020, *Sci. Adv.* **6**, eabb2307 (2020)
DOI: 10.1126/sciadv.abb2307

The PDF file includes:

Other Supplementary Material for this manuscript includes the following:

(available at advances.sciencemag.org/cgi/content/full/6/29/eabb2307/DC1)

Section S1. Descriptions of movies S1 to S6

movie S1. Comparison of contact times of bouncing water droplets on surfaces with different texture size at solid fraction Φ_s = 0.44. Water droplet bouncing kinematics were compared between surfaces with texture size D = 100 nm (left) and D = 300 nm (right). The water droplets (diameter d_0 = 2.3 mm) impacted the surfaces with a terminal velocity v = 1.0 m/s. The bouncing process was recorded by a high-speed camera at a rate of 10,000 frames per second.

movie S2. Comparison of contact times of bouncing water droplets on surfaces with different texture size at solid fraction Φ_s = 0.25. Water droplet bouncing kinematics were compared between surfaces with texture size D = 150 nm (left) and D = 400 nm (right). The water droplets (diameter d_0 = 2.3 mm) impacted the surfaces with a terminal velocity v = 1.0 m/s. The bouncing process was recorded by a high-speed camera at a rate of 10,000 frames per second.

movie S3. Pressure stability test on a reentrant micro-textured surface with solid fraction Φ_s = 0.25 and texture size D = 10 μm. The water droplet (diameter d_0 = 2.3 mm) impacted the surfaces with a terminal velocity v = 4.0 m/s. The bouncing process was recorded by a high-speed camera at a rate of 10,000 frames per second. The textured surface area is about 1 cm by 1 cm.

movie S4. Pressure stability test on a reentrant micro-textured surface with solid fraction Φ_s = 0.44 and texture size D = 10 μm. The water droplet (diameter d_0 = 2.3 mm) impacted the surfaces with a terminal velocity v = 4.0 m/s. The bouncing process was recorded by a high-speed camera at a rate of 10,000 frames per second. The textured surface area is about 1 cm by 1 cm.

movie S5. Pressure stability test on a reentrant nano-textured surface with solid fraction Φ_s = 0.25 and texture size D = 200 nm. The water droplet (diameter d_0 = 2.3 mm) impacted the surfaces with a terminal velocity v = 4.0 m/s. The bouncing process was recorded by a high-speed camera at a rate of 10,000 frames per second. The textured surface area is about 0.5 cm by 0.5 cm.

movie S6. Pressure stability test on a reentrant nano-textured surface with solid fraction Φ_s = 0.44 and texture size D = 200 nm. The water droplet (diameter d_0 = 2.3 mm) impacted the surfaces with a terminal velocity v = 4.0 m/s. The bouncing process was recorded by a high-speed camera at a rate of 10,000 frames per second. The textured surface area is about 0.5 cm by 0.5 cm.

Section S2. Fabrication of nano-/micro-scale textures

The fabrication process of nano-/micro-reentrant textures is shown in **fig. S1**. Silicon wafers with dry oxide were first coated with the photoresist ZEP520A (1:1) by a spin coater at the speed of 4000 rpm for 45 seconds. The coated wafer was then baked at 180 °C for 3 minutes. Electron beam lithography was used for transferring sub-micrometer features onto the photoresist. SiO_2 was patterned by reactive ion etching (RIE) in ULVAC NE-550 system using CF_4 plasma. The etching rate was ~ 6.3 nm per second. The etching of SiO_2 was stopped when the underneath silicon was exposed. Then isotropic reactive etching on the exposed Si was performed by SF_6 plasma in Plasma-Therm Versalock 700. The lateral etching rate was ~ 0.9 nm per second, while the vertical etching rate was ~1.4 nm per second. Finally, the photoresist residue was thoroughly cleaned by high power oxygen plasma for 10 min.

Section S3. **Design of textured surfaces**

The textured surfaces consist of pillars with a square shape arranged in a square array. The solid fraction Φ_s of textured surfaces was controlled by adjusting the texture size *D* and texture edge-to-edge spacing *S*. The solid fraction can be described by the equation $\Phi_s = D^2/(D+S)^2$ (**fig. S2**). To maintain a stable Cassie-Baxter state on these surfaces, the undercut of each pillar was carefully etched to be ~ 1/3 of the texture size *D*, and the pillar height, *H*, was designed to be much taller than the critical height, H_c, to avoid possible liquid sagging failure. Previous studies (*23*) have shown that the critical height, H_c, is a function of the pillar geometries which can be expressed as $H_c \approx 0.2\,(D+S)$. On all of our fabricated surfaces, the pillar height, $H \gg H_c$.

Section S4. Surface modification by hydrophobic silane

The fabricated textured surfaces were functionalized by chemical vapor deposition of a fluoroalkyl-silane, 1H, 1H, 2H, 2H-perfluorodecyltrimethoxysilane (FAS-17). Specifically, the fabricated samples were placed in a desiccator sealed under vacuum with 2 μL FAS-17 then heated in an oven at 120 ºC for 210 minutes. The vapor phase deposition process can consistently produce a monolayer silane coating, whose thickness was negligible compared to the dimensions of fabricated structures (~100 nm – 30 μm). We have also verified the fabricated structures under SEM and found that the dimensions of the textures were not changed after silanization. The water contact angle on a flat silicon surface became ~110° after the fluorosilanization (**fig. S3**), which approaches the theoretical maximum contact angle 120° on flat solid surfaces (*40*).

Section S5. Contact angle measurements

The difference between the measured advancing and receding angles is defined as contact angle hysteresis. The advancing and receding angles of water droplets on solid surfaces were measured by a goniometer with a CCD camera (ramé-hart, model 295, U.S.A.). Deionized water was used and the droplet

volume was precisely controlled by a programmable pump. This makes it possible to measure the advancing and receding angles using the drop-shape fitting method. As shown in **fig. S4**, a water droplet with an initial volume of 15 μL was programmed to change its volume at a rate of 1.3 μL/s by adding or removing water. The real-time contact angles during this process were recorded by the CCD camera. The advancing and receding angles can be determined by plotting the recorded contact angles as a function of time. When the volume of a water droplet is increasing, the contact line will not move outwards until the contact angle reaches its maximum, which is the advancing contact angle. Similarly, when the volume of a water droplet is decreasing, the contact line will not move inwards until the contact angle reaches its minimum, which is the receding contact angle. Therefore, the upper and lower plateaus of the contact angle curve represent advancing and receding contact angles, respectively, as shown in **fig. S4**. The advancing angle and receding angles were obtained by averaging all the measured maximum or minimum apparent contact angles during the eight cycles. On each sample, the measurements repeated at least three times to ensure accuracy. The reported contact angle hysteresis was obtained by calculating the difference between the measured advancing and receding angles.

Section S6. Droplet impact tests

Deionized water droplets with a diameter of ~2.3 mm were released using a programmable microfluidic pump (New Era Pump Systems, Inc.). The initial falling velocity was ensured to be close to zero by increasing the droplet volume slowly until the droplet detached from the needle tip by gravity. In the droplet impact tests, the releasing height h was ~ 0.05 m, and the impacting velocity can be calculated by $v = \sqrt{2gh}$, where g is the gravitational acceleration. The releasing height h was ~ 0.01 m on $\Phi_s = 0.25$ surfaces with texture size of 10 μm – 30 μm due to the poor pressure stability on these surfaces. Note that the contact time of bouncing droplets is a function of droplet size for a given liquid (*16*). In the pressure stability test, the releasing height h was ~ 0.83 m. The bouncing process was recorded by a high-speed camera (MIRO M320s, Phantom, U.S.A.) from a side view at a rate of 10,000 fps.

Section S7. Derivation of the modified contact time of bouncing droplet equation

The period of oscillation, t, of a classic spring system can be expressed as:

$$t \sim \sqrt{\frac{m}{k}} \tag{S1}$$

where m is the mass connected to a massless spring and k is the spring constant. A bouncing droplet oscillating on a surface can be considered as a liquid spring system. Previous studies (*15, 16*) on surfaces with extremely low solid fraction (i.e., Φ_s ~ 0.01) have proven that the period of a bouncing droplet interacting with solid, or contact time t_c, can be predicted by the expression:

$$t_c \sim \sqrt{\frac{\rho R^3}{\gamma}} \tag{S2}$$

where ρR^3 is the liquid spring mass. Particularly, the liquid-air surface tension γ acts as the spring constant *k,* because only ~ 1% of the solid surface is interacting with the liquid.

However, on surfaces with high solid fraction (i.e., $\Phi_s = 0.44$), the liquid-solid interaction becomes significant, and the liquid spring constant may not only be contributed by liquid-air interaction but also influenced by the liquid-solid interaction. Therefore, the effective liquid spring constant, k_e, can be approximated as $k_e = \gamma + \Phi_s \gamma cos\,\theta_r + \Lambda\tau$, where θ_r is the receding angle, Λ is the contact line density, and τ is the three-phase line tension. From our experimental measurements, θ_r is typically around 90° to 100° and therefore, $k_e \cong \gamma + \Lambda\tau$ as $\gamma >> |\Phi_s \gamma \cos\theta_r|$. The contact time of a bouncing droplet on high solid fraction surface can therefore be approximated as:

$$t_c \sim \sqrt{\frac{\rho R^3}{\gamma + \Lambda\tau}} \tag{S3}$$

where contact line density Λ can be expressed as $\Lambda = 4\Phi_s/D$. Note that equation (S3) will be reduced to equation (S2) when the texture size is on the order of micrometers and solid fraction is below 0.25 due to the low contact line density Λ.

Section S8. Pressure stability analysis on textured surfaces with straight or reentrant pillars

On a textured surface with square straight pillars (**fig. S7A**), the capillary force exerted by each pillar preventing the water-air interface from penetrating into the pillars can be analytically described as (*33*):

$$F_c = 4D\gamma|\cos\theta| \tag{S4}$$

where D is pillar side length (**fig. S2**), γ is the surface tension of water, and θ is the water contact angle on a smooth solid surface. The total capillary force within a given projected area A can be described as: $F_{total} = F_c N_p$, where $N_p = \frac{A\Phi_s}{D^2}$ is the number of pillars. The capillary pressure P_C applied at the water-air interface can be described as $P_C = \frac{F_{total}}{A(1-\phi_s)}$. After combining the above equations, the capillary pressure can be described as:

$$P_C = \frac{4\Phi_s}{1-\Phi_s}|\cos\theta|\frac{\gamma}{D} \tag{S5}$$

For a given textured surface (i.e., Φ_s and D are fixed), the maximum P_C can be achieved immediately before a pinned three-phase contact line at the pillar edge start to move (see **fig. S7A**). At this moment, the contact angle θ reaches its maximum on smooth solid surfaces, which is also known as advancing angle and it is about 120° (*40*).

On a textured surface with square reentrant pillars (**fig. S7B**), the dominating pinning position of the three-phase contact line is at the bottom edge of the pillar undercut. The bottom plane of the undercut becomes the reference plane of contact angles (*21, 39*). The capillary force exerted by each pillar preventing the water-air interface from penetrating into the pillars can be analytically described as (*21, 39*):

$$F_c = 4D\gamma|\sin\theta| \tag{S6}$$

Similar to the derivation of equation (S5), the capillary pressure P_C applied at the water-air interface can be described as:

$$P_C = \frac{4\Phi_s}{1-\Phi_s}|\sin\theta|\frac{\gamma}{D} \tag{S7}$$

For a given textured surface (i.e., Φ_s and D are fixed), the maximum P_C can be achieved when the contact angle θ equals 90°, which is the moment when the capillary force is pointing vertically upward (**fig. S7B**). Therefore, the equation (S7) is reduced to:

$$P_C = \frac{4\Phi_s}{1-\Phi_s}\frac{\gamma}{D} \tag{S8}$$

Note that the equation (S5) and (S8) also apply to circular pillars when D is defined as the pillar diameter.

When a water droplet impacts a textured surface, the pressure pushing the water-air interface downward originates from the water hammer pressure, $P_H = 0.2\rho Cv$, which results from the impact momentum of an impacting droplet, where C is the speed of sound in water (1497 m/s), and v is the terminal velocity of water droplets (*32*). By comparing the ratio between P_C and P_H, one could determine the pressure stability of the textured surfaces. For example, a typical raindrop size ranges from 1 to 3 mm, and its terminal velocity is in the range of ~2.9 m/s ≤ v ≤ ~4.9 m/s (*34*), which leads to a water hammer pressure in the range of ~0.9 MPa ≤ P_H ≤ ~1.5 MPa. To theoretically investigate the pressure stability of straight and reentrant pillars under simulated raining environment, we plotted the dimensionless pressure P^* – the ratio of maximum capillary pressure P_C and water hammer pressure P_H – as a function of texture size and solid fraction based on equation (S5) and equation (S8), respectively. Even though the pressure stability on reentrant pillars can be enhanced compared to straight pillars, both nanoscale textures (D < 1 μm) and high solid fraction (Φ_s > 0.25) are still required to sustain a capillary pressure (**fig. S9**) that is comparable to the raindrop hammer pressure (an average P_H of ~ 1.2 MPa).

Section S9. Pressure stability tests on textured surfaces with reentrant pillars

To test the pressure stability of textured surfaces under simulated raining conditions, we released water droplets with a diameter (2R) ~ 2.3 mm from a height of ~ 83 cm, which results in a terminal velocity v of ~ 4.0

m/s. The Weber number ($We = \frac{2\rho v^2 R}{\gamma}$) is about 505.5. The droplet impact process was recorded from the side using a high-speed camera at a filming rate of 10,000 Hz. The geometrical parameters of the reentrant pillars used in the pressure stability tests are shown in **table S1**.

When water droplets impact on a solid surface, there are two modes of impacting pressure. The first mode is the water hammer pressure $P_H = 0.2\rho C v$ at the contact stage, and the second mode is the dynamic pressure $P_D = 0.5\rho v^2$ at the spreading stage, where ρ is the density of water, C is the sound speed in water (1497 m/s) and v is the impact velocity (*32*). In raining conditions, water hammer pressure is much larger than the dynamic pressure (i.e., $P_H \gg P_D \sim 8$ kPa). Therefore, if the capillary pressure P_C is larger than or comparable to the water hammer pressure P_H, the droplet will remain at the Cassie-Baxter state. Previous studies showed that the water hammer pressure mainly concentrated at the center of the impact area (*32*), which indicates that if the water hammer pressure P_H is larger than the capillary pressure P_C, the droplet center will penetrate into the pillars and leads to a Wenzel state droplet. Since only the center area will be wetted, this state is defined as the partial Wenzel state (see **fig. S8D**). Full Wenzel state can be expected when the dynamic pressure P_D is also larger than the capillary pressure P_C (*32*). In our experimental conditions, we found that the dynamic pressure ($P_D \sim 8$ kPa) is smaller than the capillary pressure P_C on all four samples (see **table S1**), therefore only two wetting states will be expected in our tests, i.e., Cassie-Baxter state or partial Wenzel state (see **fig. S8**).

It is also noted that when the Weber number is as high as ~ 505.5, the droplet splashed into satellite droplets after impacting. This is because the splashing parameter $K = We\sqrt{Re} = 9652$ surpassed the splashing threshold $K_t \cong 3000$, where $Re = \frac{2\rho R v}{\mu}$ is the Reynolds number, and μ is the dynamic viscosity of water. However, in our tests the splashing does not influence the examination of wetting states at the center of the impacted areas.

Table S1. Geometrical parameters and capillary pressures of the reentrant pillars used in the pressure stability tests

Pillar Size	Solid Fraction	Capillary Pressure
200 nm	0.25	0.5 MPa
	0.44	1.2 MPa
10 μm	0.25	9.7 kPa
	0.44	22.9 kPa

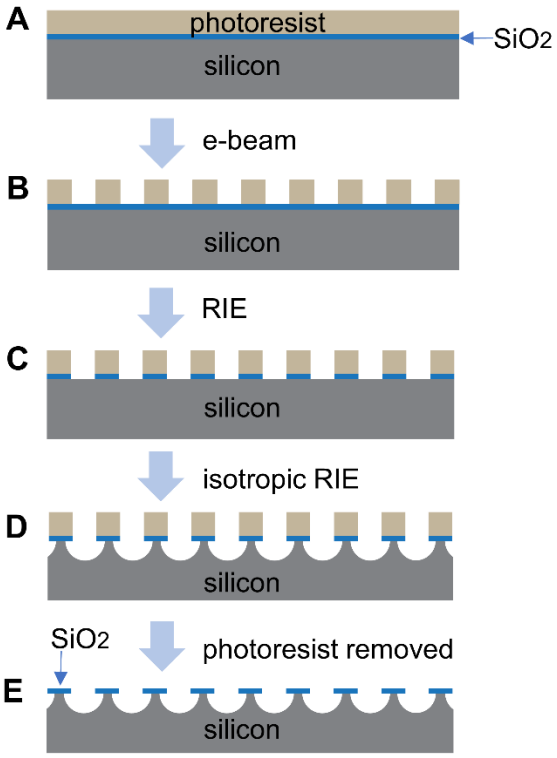

fig. S1. **Fabrication scheme of nano-/micro-scale reentrant textures. (A)** and **(B)** A silicon wafer with dry oxide was coated by photoresist and then designed patterns was transferred onto the silicon wafer by electron beam (e-beam) lithography. (**C)** Silicon dioxide was etched by reactive-ion etching (RIE) until substrate silicon exposed. (**D)** Reentrant textures were formed by isotropic reactive-ion etching over the exposed silicon. (**E)** Photoresist residue was removed by oxygen plasma cleaning. For larger reentrant textures with texture size of 5 – 30 μm, ultra-violet (365 nm) photolithograph was used in step (**A)** and **(B)**.

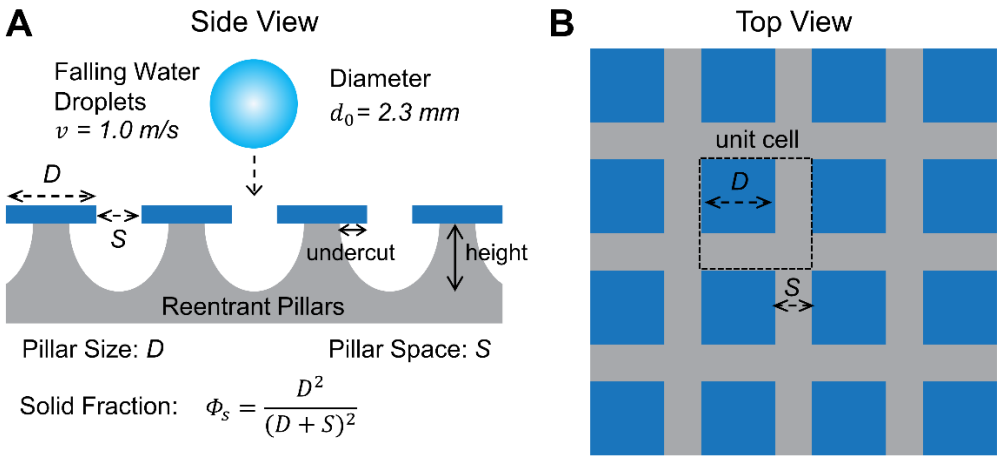

fig. S2. Schematic illustration of textured surfaces with reentrant textures. (A) A side view showing a water droplet impacting a textured surface. The texture size is defined as *D* and the texture edge-to-edge space is defined as *S*. **(B)** Top view of the textured surface. The size of the unit cell equals the sum of *D* and *S*. The solid fraction of a textured surface is defined by *D* and *S*. The water droplets diameter is defined as d_0.

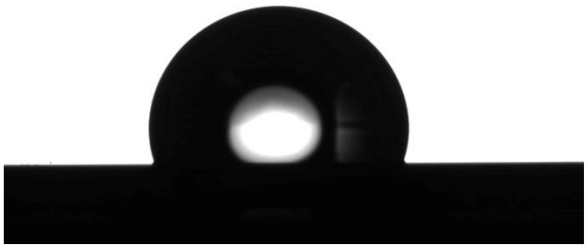

fig. S3. Water contact angle on a FAS-17 modified flat silicon dioxide surface. An optical image showing a 10 μL water droplet resting on a FAS-17 modified flat silicon dioxide surface with a static contact angle of ~ 110°.

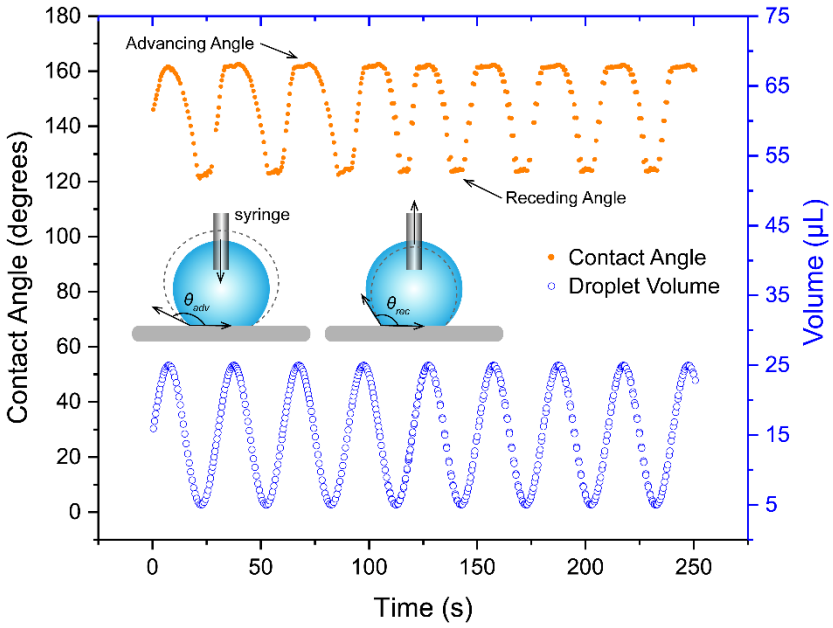

fig. S4. **Measured water advancing angles and receding angles on a representative textured surface.** The drop-shape fitting method was used, which is a method plotting the measured contact angles along with droplet volume changes. The upper plateau of measured contact angle is advancing contact angle and the lower plateau is receding contact angle.

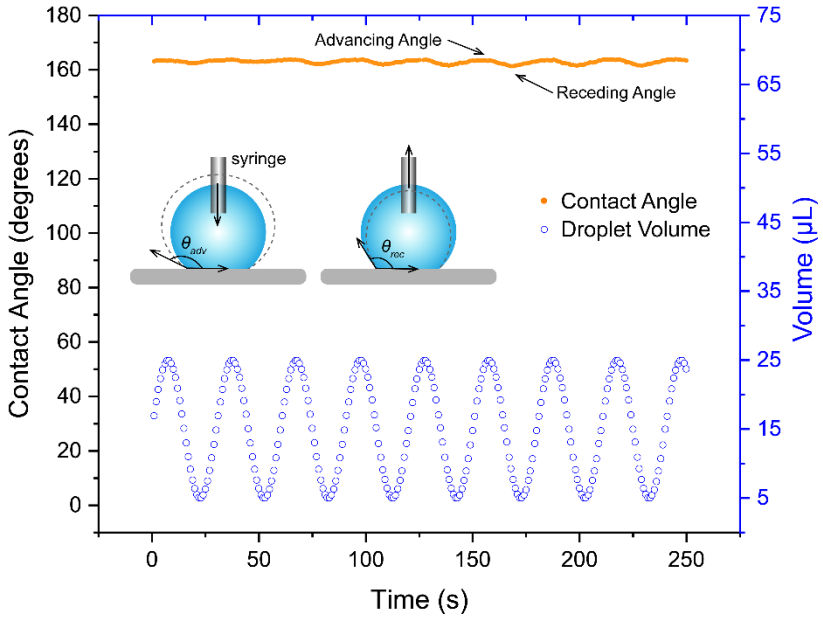

fig. S5. Measured water advancing and receding angles on a black silicon surface. The drop-shape fitting method was used, which is a method plotting the measured contact angles along with droplet volume changes. The upper plateau of measured contact angle is advancing contact angle and the lower plateau is receding contact angle. The contact angle hysteresis of black silicon is determined to be 1.6±0.5°.

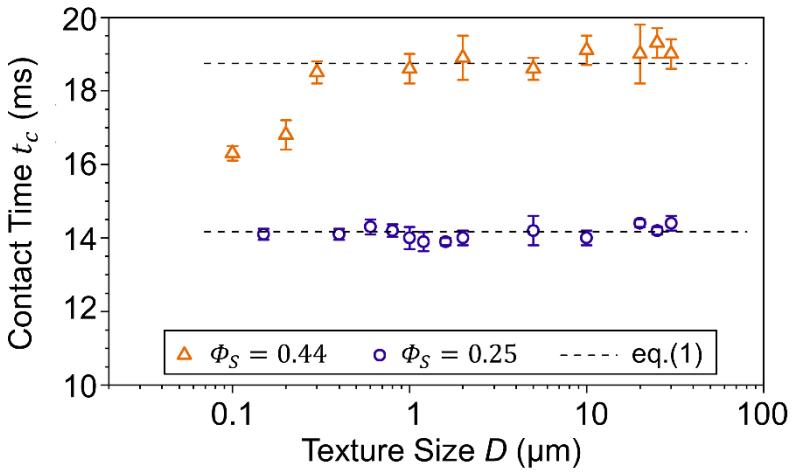

fig. S6. Comparison between the measured contact time t_c of bouncing droplets and those predicted by a conventional theory. The dash lines are predictions from equation (1), $t_c = a\sqrt{\rho R^3/\gamma}$, where ρ, γ are the density and surface tension of water, respectively; a is an empirical pre-factor determined from experiments. The purple circles and the orange triangles represent the measured contact time obtained from surfaces at Φ_s = 0.25 and Φ_s = 0.44, respectively. Error bars represent the standard deviations of three independent measurements.

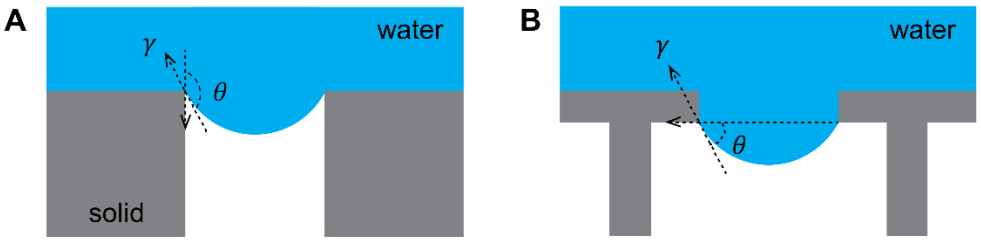

fig. S7. Schematic illustration of pressure stability on straight and reentrant pillars. Water advancing into the gaps between **(A)** straight pillars and **(B)** reentrant pillars, where γ is the surface tension of water and θ is water contact angle on a smooth solid surface. When the pressure inside the water (for example, water hammer pressure) is larger than the capillary pressure at the water-air interface, the three-phase contact line will be depinned, and will move downward on straight pillars or move outward on reentrant pillars.

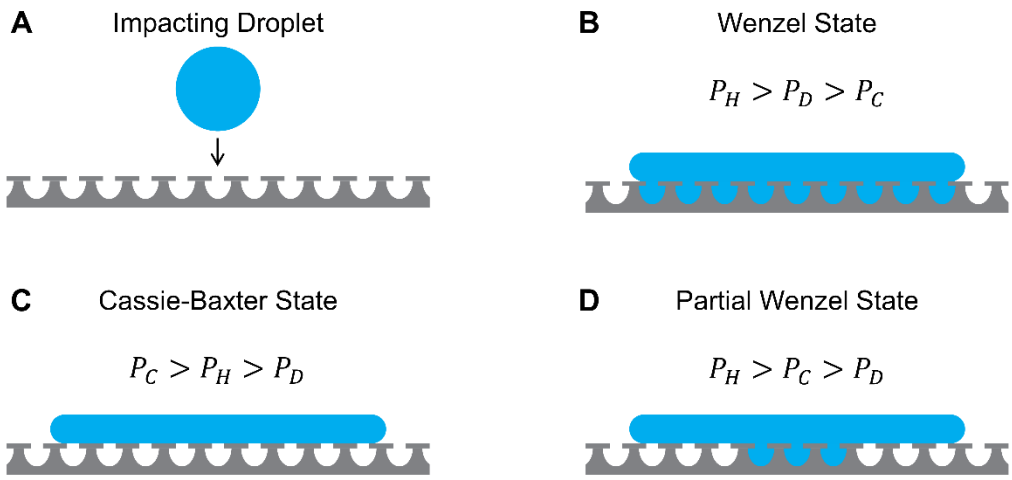

fig. S8. Schematic illustrations of a water droplet impacting on textured surfaces at various impact pressures. (A) A schematic showing a water droplet impacting onto a textured surface at a certain velocity. **(B)** Wenzel state droplet: if the capillary pressure P_C is smaller than both the water hammer pressure P_H and the dynamic pressure P_D, the droplet will penetrate into the pillars, leading to a Wenzel state. **(C)** Cassie-Baxter state droplet: if the capillary pressure P_C is larger than the water hammer pressure P_H, the droplet maintains a Cassie-Baxter state. **(D)** Partial Wenzel state droplet: if the capillary pressure P_C is smaller than the water hammer pressure P_H but is larger than the dynamic pressure P_D, the droplet center will penetrate into the pillars, leading to a partial Wenzel state. (*32*)

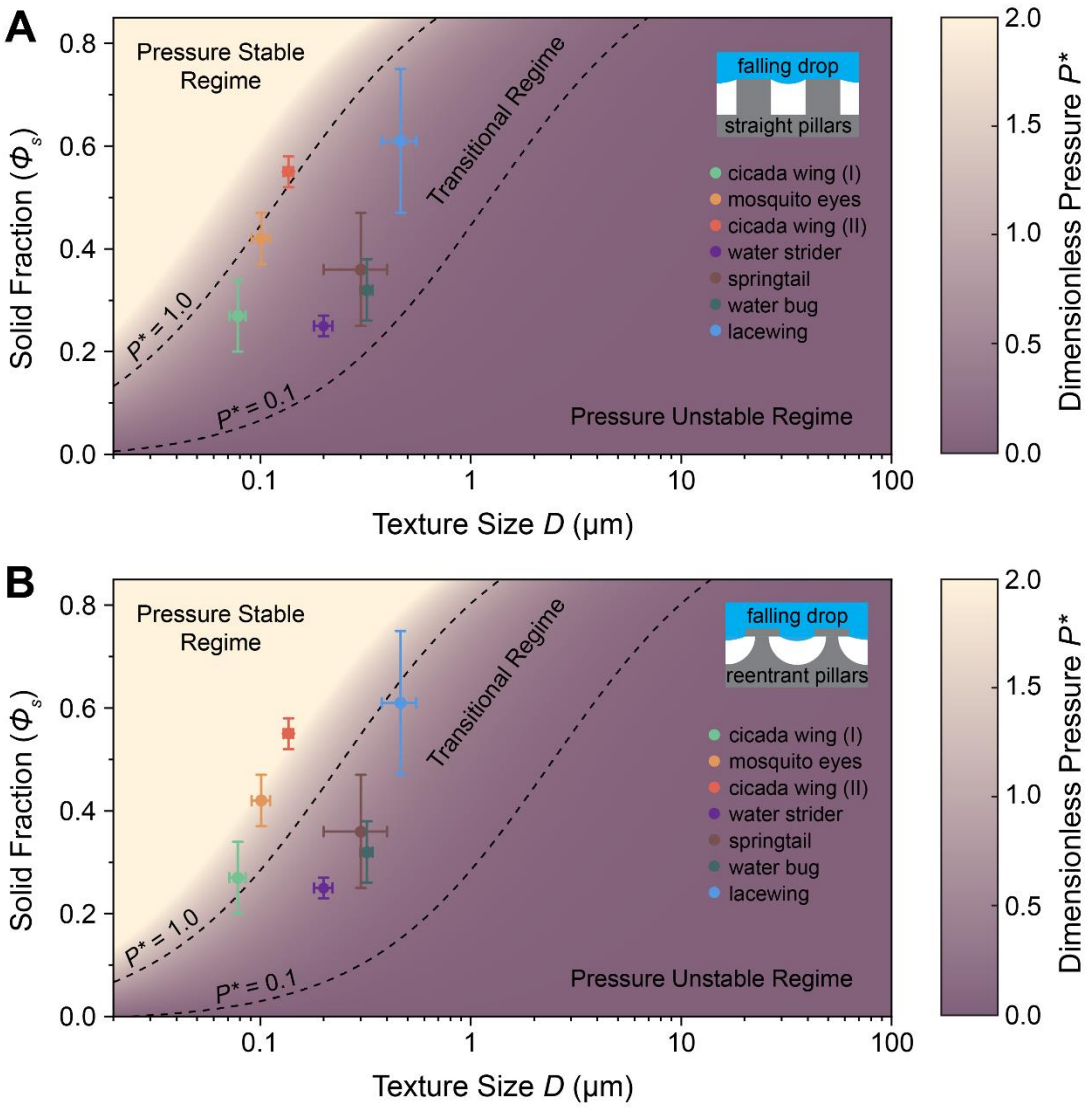

fig. S9. Phase maps showing the pressure stability of (A) straight and (B) reentrant pillars against impacting raindrops as a function of the texture size and solid fraction. To repel impacting raindrops, it requires a sufficient capillary pressure P_C on textured surfaces to withstand the raindrop hammer pressure P_H. P^* is defined as the ratio between P_C and P_H, i.e., $P^* = P_C/P_H$. Note that the textured surfaces are pressure stable when texture size D is small at high solid fraction Φ_s. It is shown that all the geometrical parameters of the surface textures on water-repellent insects fall within or near the pressure stable regime.

REFERENCES AND NOTES

1. A. B. D. Cassie, S. Baxter, Large contact angles of plant and animal surfaces. *Nature* **155**, 21–22 (1945).

2. A. B. D. Cassie, S. Baxter, Wettability of porous surfaces. *Trans. Faraday Soc.* **40**, 546–551 (1944).

3. W. Barthlott, C. Neinhuis, Purity of the sacred lotus, or escape from contamination in biological surfaces. *Planta* **202**, 1–8 (1997).

4. T. Wagner, C. Neinhuis, W. Barthlott, Wettability and contaminability of insect wings as a function of their surface sculptures. *Acta Zoologica* **77**, 213–225 (1996).

5. F. van Breugel, M. H. Dickinson, Superhydrophobic diving flies (*Ephydra hians*) and the hypersaline waters of mono lake. *Proc. Natl. Acad. Sci. U.S.A.* **114**, 13483–13488 (2017).

6. X. Gao, X. Yan, X. Yao, L. Xu, K. Zhang, J. Zhang, B. Yang, L. Jiang, The dry-style antifogging properties of mosquito compound eyes and artificial analogues prepared by soft lithography. *Adv. Mater.* **19**, 2213–2217 (2007).

7. H. Gundersen, H. P. Leinaas, C. Thaulow, Surface structure and wetting characteristics of collembola cuticles. *PLOS ONE* **9**, e86783 (2014).

8. J. Oh, C. E. Dana, S. Hong, J. K. Román, K. D. Jo, J. W. Hong, J. Nguyen, D. M. Cropek, M. Alleyne, N. Miljkovic, Exploring the role of habitat on the wettability of cicada wings. *ACS Appl. Mater. Interfaces* **9**, 27173–27184 (2017).

9. G. S. Watson, J. A. Watson, B. W. Cribb, Diversity of cuticular micro- and nanostructures on insects: Properties, functions, and potential applications. *Annu. Rev. Entomol.* **62**, 185–205 (2017).

10. P. B. Clapham, M. C. Hutley, Reduction of lens reflexion by the "Moth Eye" principle. *Nature* **244**, 281–282 (1973).

11. T. Mouterde, G. Lehoucq, S. Xavier, A. Checco, C. T. Black, A. Rahman, T. Midavaine, C. Clanet, D. Quéré, Antifogging abilities of model nanotextures. *Nat. Mater.* **16**, 658–663 (2017).

12. K. M. Wisdom, J. A. Watson, X. Qu, F. Liu, G. S. Watson, C.-H. Chen, Self-cleaning of superhydrophobic surfaces by self-propelled jumping condensate. *Proc. Natl. Acad. Sci. U.S.A.* **110**, 7992–7997 (2013).

13. E. P. Ivanova, J. Hasan, H. K. Webb, G. Gervinskas, S. Juodkazis, V. K. Truong, A. H. F. Wu, R. N. Lamb, V. A. Baulin, G. S. Watson, J. A. Watson, D. E. Mainwaring, R. J. Crawford, Bactericidal activity of black silicon. *Nat. Commun.* **4**, 2838 (2013).

14. A. K. Dickerson, P. G. Shankles, N. M. Madhavan, D. L. Hu, Mosquitoes survive raindrop collisions by virtue of their low mass. *Proc. Natl. Acad. Sci. U.S.A.* **109**, 9822–9827 (2012).

15. J. C. Bird, R. Dhiman, H.-M. Kwon, K. K. Varanasi, Reducing the contact time of a bouncing drop. *Nature* **503**, 385–388 (2013).

16. D. Richard, C. Clanet, D. Quéré, Contact time of a bouncing drop. *Nature* **417**, 811 (2002).

17. Y. Liu, L. Moevius, X. Xu, T. Qian, J. M. Yeomans, Z. Wang, Pancake bouncing on superhydrophobic surfaces. *Nat. Phys.* **10**, 515–519 (2014).

18. R. N. Wenzel, Resistance of solid surfaces to wetting by water. *Ind. Eng. Chem.* **28**, 988–994 (1936).

19. T.-S. Wong, C.-M. Ho, Dependence of macroscopic wetting on nanoscopic surface textures. *Langmuir* **25**, 12851–12854 (2009).

20. J. W. Gibbs, *The scientific papers of J. Willard Gibbs* (Dover Publications, 1961).

21. A. Tuteja, W. Choi, M. Ma, J. M. Mabry, S. A. Mazzella, G. C. Rutledge, G. H. McKinley, R. E. Cohen, Designing superoleophobic surfaces. *Science* **318**, 1618–1622 (2007).

22. T. Y. Liu, C.-J. C. J. Kim, Turning a surface superrepellent even to completely wetting liquids. *Science* **346**, 1096–1100 (2014).

23. J. R. Panter, Y. Gizaw, H. Kusumaatmaja, Multifaceted design optimization for superomniphobic surfaces. *Sci. Adv.* **5**, eaav7328 (2019).

24. X. Li, X. Ma, Z. Lan, Dynamic behavior of the water droplet impact on a textured hydrophobic/superhydrophobic surface: The effect of the remaining liquid film arising on the pillars' tops on the contact time. *Langmuir* **26**, 4831–4838 (2010).

25. E. Y. Bormashenko, *Wetting of real surfaces* (De Gruyter, Berlin, 2013).

26. A. Amirfazli, A. W. Neumann, Status of the three-phase line tension: A review. *Adv. Colloid Interface Sci.* **110**, 121–141 (2004).

27. H. Gundersen, H. P. Leinaas, C. Thaulow, Collembola cuticles and the three-phase line tension. *Beilstein J. Nanotechnol.* **8**, 1714–1722 (2017).

28. A. Marmur, Line tension and the intrinsic contact angle in solid–liquid–fluid systems. *J. Colloid Interface Sci.* **186**, 462–466 (1997).

29. D. Quéré, Model droplets. *Nat. Mater.* **3**, 79–80 (2004).

30. C. Clanet, C. Béguin, D. Richard, D. Quéré, Maximal deformation of an impacting drop. *J. Fluid Mech.* **517**, 199–208 (2004).

31. D. Öner, T. J. McCarthy, Ultrahydrophobic surfaces. Effects of topography length scales on wettability. *Langmuir* **16**, 7777–7782 (2000).

32. T. Deng, K. K. Varanasi, M. Hsu, N. Bhate, C. Keimel, J. Stein, M. Blohm, Nonwetting of impinging droplets on textured surfaces. *Appl. Phys. Lett.* **94**, 133109 (2009).

33. D. Bartolo, F. Bouamrirene, É. Verneuil, A. Buguin, P. Silberzan, S. Moulinet, Bouncing or sticky droplets: Impalement transitions on superhydrophobic micropatterned surfaces. *Europhys. Lett.* **74**, 299–305 (2006).

34. E. Villermaux, B. Bossa, Single-drop fragmentation determines size distribution of raindrops. *Nat. Phys.* **5**, 697–702 (2009).

35. R. Ortega, N. Bhadelia, O. Obanor, K. Cyr, P. Yu, M. McMahon, D. Gotzmann, Putting on and removing personal protective equipment. *N. Engl. J. Med.* **372**, e16 (2015).

36. D. Floreano, R. J. Wood, Science, technology and the future of small autonomous drones. *Nature* **521**, 460–466 (2015).

37. H.-M. Hu, J. A. Watson, B. W. Cribb, G. S. Watson, Fouling of nanostructured insect cuticle: Adhesion of natural and artificial contaminants. *Biofouling* **27**, 1125–1137 (2011).

38. P. Ditsche-Kuru, E. S. Schneider, J.-E. Melskotte, M. Brede, A. Leder, W. Barthlott, Superhydrophobic surfaces of the water bug *Notonecta glauca:* A model for friction reduction and air retention. *Beilstein J. Nanotechnol.* **2**, 137–144 (2011).

39. R. Hensel, R. Helbig, S. Aland, H.-G. Braun, A. Voigt, C. Neinhuis, C. Werner, Wetting resistance at its topographical limit: The benefit of mushroom and serif T structures. *Langmuir* **29**, 1100–1112 (2013).

40. T. Nishino, M. Meguro, K. Nakamae, M. Matsushita, Y. Ueda, The lowest surface free energy based on $-CF_3$ alignment. *Langmuir* **15**, 4321–4323 (1999).